Reflectivity and emissivity analysis of thermoplastic CFRP for optimising Xenon heating and thermographic measurements

Meister, Sebastian; Kolbe, Andreas; Groves, Roger M.

DOI
10.1016/j.compositesa.2022.106972

Publication date
2022

Document Version
Final published version

Published in
Composites Part A: Applied Science and Manufacturing

Citation (APA)
Meister, S., Kolbe, A., & Groves, R. M. (2022). Reflectivity and emissivity analysis of thermoplastic CFRP for optimising Xenon heating and thermographic measurements. *Composites Part A: Applied Science and Manufacturing*, *158*, Article 106972. https://doi.org/10.1016/j.compositesa.2022.106972

Composites: Part A 158 (2022) 106972

Contents lists available at ScienceDirect

Composites Part A

journal homepage: www.elsevier.com/locate/compositesa

Reflectivity and emissivity analysis of thermoplastic CFRP for optimising Xenon heating and thermographic measurements

Sebastian Meister [a,b,*], Andreas Kolbe [a], Roger M. Groves [b]

[a] Center for Lightweight Production Technology (ZLP), German Aerospace Center (DLR), Ottenbecker Damm 12, Stade, 21680, Germany
[b] Aerospace Non-Destructive Testing Laboratory, Delft University of Technology, Kluyverweg 1, Delft, 2629, The Netherlands

ARTICLE INFO

Keywords:
Electrical properties
Optical properties/techniques
Process monitoring
Automated fibre placement (AFP)

ABSTRACT

The demand for efficient composite production processes is growing as the proportion of composites in modern aircraft increases. Particularly, thermoplastic composites are interesting for sustainability and cost efficiency. They can be manufactured using deposition methods, which involve heating by radiation in the visible and near-infrared spectra. A Xenon flashlamp is a commonly used for manufacturing. In-line inspection can be performed using thermographic cameras which measure infrared radiation. For those, the composite's angle-dependent reflection and emission behaviour is interesting. Accordingly, the relationships between angle and temperature dependent visible/near-infrared reflectivity and thermal infrared emissivity is investigated and composite's conductivity properties are derived. The link between the material's optical and electromagnetic properties is estimated through the Brewster angle derived from Fresnel fitting, which allows the prediction of the directional electrical and thermal conductivity by non-contact measurement. The findings from this study will be valuable for users of Xenon heating and thermographic measurement systems.

1. Introduction

The current application of *Carbon Fiber Reinforced Plastic* (CFRP) in aircraft types such as A350 or B787 is evident from Refs. [1,2]. To enable efficient CFRP component production and to meet the future demand for composite parts *Automated Fiber Placement* (AFP) technology is a promising approach. This technique can be utilised flexibly for various manufacturing processes [3] and the fabrication of complex components is possible with this technology [4]. In particular AFP processes for thermoplastic CFRP manufacturing have certain advantages [5], especially for sustainability and recycling [6], as in-situ consolidation and the weldability of these thermoplastic materials offer potential savings in terms of energy and costs [5]. To process such materials, they need to be heated, dependent on the material, up to 410 °C during fibre placement [7,8]. One option for heating is the Xenon flashlamp. This heating device makes use of pulsed Xenon light in the *Visible light* (VIS) and *Near-Infrared* (NIR) spectrum which is projected onto the substrate in order to heat fibre material laid on a mould [9]. As an example, the emission spectrum for a Heraeus Noblelight Humm3® Xenon flashlamp in the visible and near-infrared is shown in Fig. 1. [10] Due to the lamp characteristic, however, radiation of lower intensity is also emitted in the NIR domain [11]. For quality control of the deposited material it is essential to monitor the temperature of the CFRP material during the heating process. For this purpose, a thermographic camera is frequently installed on top of the AFP effector, to measures the intensity of the thermal *Infrared* (IR) radiation [12–15]. Thus, the interaction of the thermoplastic CFRP material in the VIS, NIR and *Far-Infrared* (FIR) spectral ranges are of huge interest for manufacturing processes and monitoring [16–18]. In our study, we will examine the angle-dependent reflectance behaviour of a rather novel *Low Melt* (LM)-*Polyaryletherketone* (PAEK) CFRP *unidirectional* (UD) fibre material in the 400–700 nm and 1300––1800 nm spectral ranges with a Goniometer. These wavelength blocks will be investigated as they are representative spectral regions for the VIS and NIR range in the Xenon spectrum. Furthermore, the relative, angle-dependent emissivity of the material in the FIR range of 7.5–13 μm will be investigated as a typical spectral range for the in-line thermographic measurements [19]. During the measurements, the detection, illumination and fibre orientations are varied. Following this analysis, we will aim to answer the following research questions:

I. Which correlations are apparent between the angular reflectance characteristics for the VIS and NIR spectral range versus its radiation behaviour of thermal FIR radiation for UD LM-PAEK thermoplastic CFRP material, especially when considering fibre orientation?

* Corresponding author at: Aerospace Non-Destructive Testing Laboratory, Delft University of Technology, Kluyverweg 1, Delft, 2629, The Netherlands.
E-mail address: sebastian.meister@dlr.de (S. Meister).

https://doi.org/10.1016/j.compositesa.2022.106972
Received 19 July 2021; Received in revised form 15 April 2022; Accepted 21 April 2022
Available online 4 May 2022

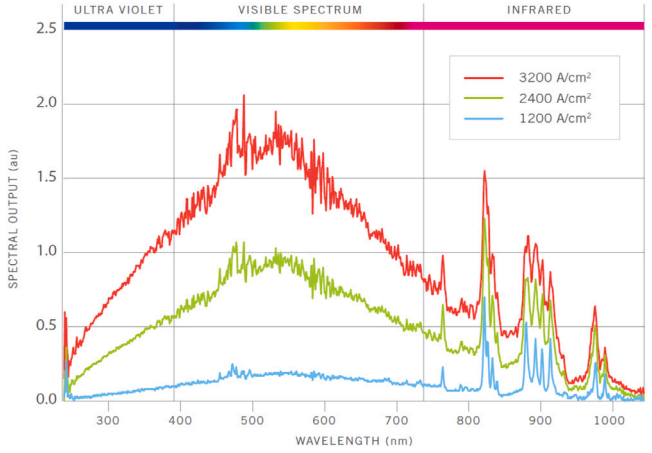

Fig. 1. The figure illustrates the characteristic spectrum of the Humm3® Xenon flashlamp from the company Heraeus Noblelight Ltd. for different operating currents (A) for the wavelength interval $[200, 1100]$ nm.
Source: This diagram is taken from [10].

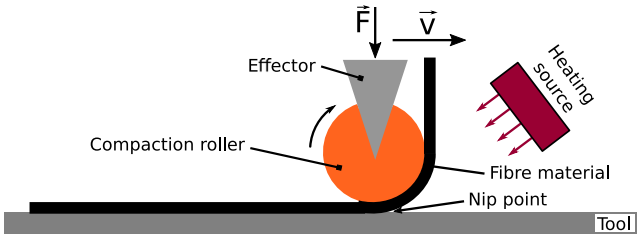

Fig. 2. Fibre placement procedure with effector, heating system and compaction roller. $\vec{F}$ denotes the compaction force and $\vec{v}$ the layup velocity. The layup point (nip point) is highlighted.

II. How can such information be used to optimise the heating of the fibre material with a flashlamp and to monitor the manufacturing process via thermographic imaging?

2. Related research

2.1. Manufacturing process and heating system

A very popular fibre deposition technique is the AFP approach. Modern AFP machines consist of a layup head with a creel and a kinematic system such as an industrial robot or a gantry. The layup head has the ability to clamp, feed, cut and restart each tow individually. For the deposition of PAEK, lay up velocities of up to 100 $\frac{m}{min} \approx 1.67 \frac{m}{s}$ are achievable [20]. For thermoset materials current developments aim to achieve linear lay up speeds of up to 3 $\frac{m}{s}$ in future applications [21,22]. Such a fibre depositioning machine is schematically illustrated in Fig. 2. During layup the effector continuously delivers material from material storage to the layup point at the so-called nip point. At this position, the material is heated by a heating source and compressed by a compaction roller to consolidate the thermoplastic material and remove voids within the produced laminate. For thermoplastic AFP processes, PAEK based CFRP offers particularly beneficial processing properties, such as a wide range of processing temperatures between 340 °C and 400 °C depending on the layup quality to be achieved [23]. To achieve in-situ consolidation, nip point temperatures of up to 410 °C have been reported in literature [8]. However, it should be kept in mind that the degree of consolidation is controlled by the time and pressure the material is exposed to at a certain temperature. To generate the temperatures required for accurate thermoplastic depositioning, a wide variety of heating sources have been developed and investigated over the years, including hot gas torch heating, infrared heating and *Laser Assisted Tape Placement* (LATP) processing of thermoplastics [22,24–26]. Luinge [27] and Schiel et al. [8] in particular outlined suitable LATP processing methods for PAEK. A majority of studies have focused on thermal modelling of the LATP process for thermoplastics [28–30]. In addition to hot gas torch heating, infrared heating and laser heating solutions as described above, Xenon flashlamp heating sources have alsp been developed in the past years for AFP processing [7,31]. A Xenon flashlamp consists of a quartz glass tube with a metallic anode and cathode, filled with pressurised Xenon gas. By applying a voltage above the lamp's breakdown voltage the Xenon gas transforms into a plasma. In contrast to lasers, flashlamp systems emit pulsed broadband radiation spectrum. Brown et al. [32] investigated the emitted flashlamp spectrum in the spectral range between 250 nm and 1050 nm. This is roughly the range where the most energy is emitted, however the actual Xenon spectrum extends much further into the NIR region [11]. Depending on the setting of the individual pulse parameters intensity, duration and frequency, the lamp transfers the energy differently to the material which opens up the opportunity to perform fine adjustments on the nip point temperature. To address this, Monnot et al. [33] have reported a semi-empirical heat transfer model based on steady state nip point temperatures to predict the nip point temperature for dry fibre placement with a Xenon flashlamp. Additionally, Danezis et al. [9] have developed a combined modelling approach where ray tracing data was used as an input for their 2D finite element heat conduction model. This allowed an analysis of the temperature field evolution based on short high energy pulses. Extending these finite modelling approaches by considering optical material properties should offer the potential to increase the prediction accuracy of nip point temperatures.

2.2. Thermographic temperature monitoring

Usamentiaga et al. [34] summarised the functional principles of a thermographic sensor as well as the fundamental mathematical and functional relationships for different wavelength ranges. In addition, they outlined various applications for thermographic camera-based monitoring in composite manufacturing. Oromiehie et al. [35] presented an approach for thermographic temperature measurements to enable the deviation of the thermomechanical properties of thermoplastic CFRP.

2.3. Principles for measuring optical material properties

Rabal et al. [36] presented a hemispherical determination of reflectivity within a spectral interval ranging from 380 nm to 780 nm and at a spectral precision of 0.3 nm. Martinez and Hartmann [37] performed similar measurements as well. The Goniometer they used for their experiments yields spectrally resolved measurements in the interval from 240 nm to 2000 nm, and they achieved a resolution of 15 bit with a spectral uncertainty of 3 nm. Li et al. [38] performed spectroradiometric measurements in the band from 380 nm to 760 nm using 1024 individual bins. Their spectral resolution varies within the range 0.82 nm to 3.3 nm. In summary, from the presented literature we conclude that a Goniometer is very well suited to characterise the optical properties of various materials for different applications.

2.4. Optical, thermal and electrical properties of composite materials

2.4.1. Reflectivity

Xu et al. [39] examined the scattering characteristics of an individual fibre, which built on the studies of Schmitt et al. [40]. On the basis of the investigations of Grouve [41], Stokes-Griffin and Compston [42] provided a qualitative analysis of the reflection properties of UD CFRP material, where they described the accumulated reflectance properties of multiple mono-filaments of similarly aligned fibres. They found that,

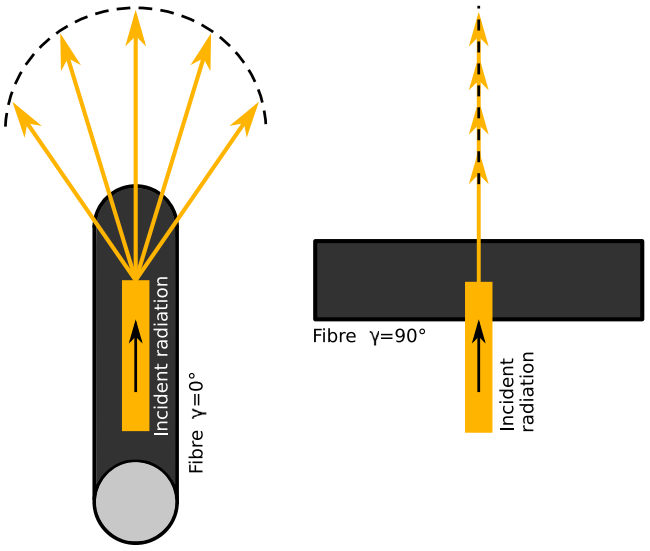

Fig. 3. Irradiation reflection model for a single fibre and two filament orientations $\gamma = 0°$ and $\gamma = 90°$.

for the VIS and up to a irradiation wavelength of 980 nm, these can be considered as an individual large cylinder. This is only valid if the observed object is significantly larger than the illumination wavelength, as otherwise additional optical effects can occur. The reported idea of a scattering large cylinder is schematically presented in Fig. 3. In this figure both extreme scenarios of a filament rotation of $\gamma = 0°$ and a filament rotation of $\gamma = 90°$ are illustrated. Consider a filament angle of $\gamma = 0°$, in this case the cylindrical body is illuminated angled from above, parallel to the filament orientation. When a diffuse target is positioned directly behind the cylindrical object in such a way that the diffuse target's normal is aligned to be parallel with the cylindrical body, the reflection of the given illumination of the cylindrical object results in a semi-circular image on the target. On the other hand, when the position and orientation of the diffuse target and the direction of the incoming light beam stay unchanged, but the cylindrical surface is turned to $\gamma = 90°$, a straight vertical line appears on the target.

Stokes-Griffin and Compston [42] also explained in detail the interaction between the composite and an incident laser. In their study, they analysed the optical characteristics of thermoplastic CFRP for NIR laser heating. Therefore, they investigated different absorption characteristics of the composite. Le Louët et al. [16] studied the bi-directional reflectivity characteristics of a *Polyetheretherketone* (PEEK) based CFRP in the spectral range from 600 nm to 25 µm. For this, they investigated temperatures in the range 20–450 °C. They judged that the influence of the fibre on the optical material properties was significantly larger than that of the polymer matrix and they also emphasised the anisotropy of the material, due to the alignment of the filaments. Baho et al. [18] investigated the angle-dependent reflection behaviour as well as the penetration depth of a laser with the wavelength $\lambda = 980$ nm for a thermoplastic fibre composite material. Furthermore, they analysed the refractive index of the material in the wavelength range between 500 and 1100 nm and examined the density-dependent thermal conductivity of the material in the context of a fibre placement process. Based on this, they derived a heat propagation model depending on the laser power and lay up velocity.

2.4.2. Refraction of light

When a composite is irradiated, a part of the light is reflected and the remaining part propagates within the material. The proportion of the reflected to the transmitted irradiance varies with the lighting angle. For objects much lager than the wavelength this is described through the following Snells law:

$$n_a \sin(\beta) = n_c \sin(\theta_c) \tag{1}$$

This formula considers the angle of incidence β, the angle of refraction θ_c and the refractive indices n_i for a ray transitioning between two connected isotropic media [42,43]. On this basis, the critical angle of incidence β_R for which $\theta_c = 90°$ can be determined as:

$$\beta_R = \arcsin(\frac{n_c}{n_a}) \tag{2}$$

When the incidence angle is larger than β_R the incident radiation is entirely reflected [42,43]. From this, the Brewster angle θ_B can be derived, which specifies the critical angle at which the p-polarised part of the incident radiation is no longer reflected. This Brewster angle θ_B is defined as follows: [43,44]

$$\theta_B = \arctan(\frac{n_c}{n_a}) \tag{3}$$

However, Snell's law only applies to the transfer of rays between isotropic media. Therefore, this equation is only partially applicable for CFRP. As stated above, the law only applies at the macroscopic level, when the wavelength under consideration is outside the order of magnitude of a grating for example one formed by the carbon fibres. Thus, this law applies to CFRP for the interface between the air and the matrix material. In the VIS and NIR spectrum for the interface between matrix material and filaments its validity is already limited, depending on the filament diameter. For this interface the law is no longer valid in the FIR spectrum, since the filament diameter is within the order of magnitude of the observation wavelength.

The Fresnel equation describes the reflection and transmission properties of electromagnetic irradiation at the interface between two optical media. Therefore, the relative reflectances R_s and R_p for the *s*- and *p*-polarised radiation, respectively, are:

$$\begin{aligned} R_s &= \left(\frac{n_a \cos(\beta) - n_c a}{n_a \cos(\beta) + n_c a}\right)^2, \\ R_p &= \left(\frac{n_a a - n_c \cos(\beta)}{n_a a + n_c \cos(\beta)}\right)^2, \text{ with} \\ a &= \sqrt{1 - \left(\frac{n_a}{n_c}\sin(\beta)\right)^2} \\ R_e &= \frac{R_s + R_p}{2} \end{aligned} \tag{4}$$

R_e represents the effective reflectance, which is the mean value of R_s and R_p [43,45]. Furthermore, the emissivity E can be calculated by: [44,46]

$$E = 1 - R - T_c \tag{5}$$

where R denotes the reflected and T_c is the transmitted proportion of the total radiation. For thick thermoplastic CFRP materials, usually $T_c = 0$ can be assumed. [9]

2.4.3. Emissivity

Adibekyan et al. [17] focused on the spectral emissivity analysis of different fibre composite materials in the IR spectrum from 5 µm to 25 µm. They investigated the material emissivity properties for various viewing angles between 10° and 70°. Furthermore, they examined the material's perpendicular reflectivity and transmissivity characteristics from 1.0 µm to 16.7 µm at 40 °C, as a nominal sample temperature for their experiments. Li and Strieder [47] investigated the emissivity properties of CFRP especially with respect to fibre diameter and the gap between the individual filaments. They also found that the material's temperature probably has only a small influence on the change in FIR emissivity coefficient, but due to Planck's law, the emissivity of the material changes slightly with the temperature. Accordingly, as the temperature rises, the spectral peak of the emissivity would be expected

to drift to a shorter wavelength [43]. With the aim of determining the emissivity, Nunak et al. [48] outlined a pragmatic approach for emissivity estimation with a thermographic camera. Tomboulian and Hyers [49] studied the impact of the volume fraction of the composite material on its absorption, reflection and transmission behaviour using the reverse Monte-Carlo Ray-Tracing approach for different emissivity coefficients ranging from $\epsilon = 0.6$ to $\epsilon = 0.9$. They found, that for a volume fraction >10%, the effective emissivity decreases with increasing volume fraction, but for fibre volume fractions ≤10%, the emissivity increases very quickly from 0.05 to between $\epsilon = 0.75$ and $\epsilon = 0.95$. The effective transmission can be assumed to be approximately $T_c = 0$ above a fibre volume fraction of 20%, as for a smaller fibre volume fraction the effective transmission drops very steeply and non-linearly from $T_c = 0.95$ at 0%. The effective reflectivity rises from 0.0 to 0.1 at around 1% fibre volume fraction and then increases linearly to around 0.2 at 90% fibre volume fraction. Warren et al. [46] studied the angle dependant change in emissivity coefficient and respective Fresnel fitting for the emissivity of rough surfaces. Moreover, they compared the outcomes of the Fresnel fitting with a Monte-Carlo Ray-Tracing approach, which they found fitted slightly more accurately to their data. Golyk et al. [50] analysed the heat radiation of long cylinders with respect to various wavelength in the thermal IR band. This research is especially valuable in combination with the research of Stokes-Griffin [42] and Grouve [41] which modelled multiple individual carbon filaments as one large cylinder.

2.4.4. Thermal and electrical conductivity

Vollmer and Möllmann [44] outlined the difference in the Fresnel shape of the angular emissivity of electrically conductive and non-conductive materials. They explained that the curved shape of the angular emissivity for conductive materials follows more closely the p-polarised Fresnel plot, while non-conductive materials follow the effective or even the s-polarised Fresnel curve. Ebbesen et al. [51] have described the linear decrease of the electrical resistance of a single carbon fibre with increasing temperature. For carbon fibres the electrical conductivity σ_{el} is approximately proportional to the reciprocal value of the resistance: $\sigma_{el} \sim \frac{1}{R}$ [52]. Accordingly, Wang et al. [53] as well as Mohiuddin and Hoa [52] showed that the conductivity of carbon fibre increases exponentially with increasing temperature. Zhao et al. [54] reviewed the electrical conductivity and resistance of multiple stacked composite layers in all three dimensions. They also described the linear proportional decrease of the electrical conductivity of CFRP when it is rotated from the angle of highest conductivity in the direction of the fibres to the orientation of lowest conductivity transverse to the direction of the fibres. Majérus et al. [55] studied the link between the Brewster angle for the reflectivity of a material in the VIS as well as NIR spectra in the spectral band [250 to 950] nm and their influence on the material's two dimensional electrical conductivity. They used a glass substrate with different numbers of conductive graphene layers for their experiments and found, that the Brewster angle for the reflection of VIS and NIR rises with increasing two dimensional electrical conductivity of the material. In particular, they specify the Brewster angle shift $\Delta\theta_B$ for the spectral range [750 to 950] nm as:

$$\Delta\theta_B \epsilon_0 c \approx \frac{1}{2}\frac{n_a}{n_c^2}\sigma_{el,0} \tag{6}$$

In this equation ϵ_0 denotes the vacuum permittivity of the material and c gives the electrolyte concentration. Accordingly, ϵ_0 and c are almost constant. Since σ_{el} changes with temperature, a known base electrical conductivity $\sigma_{el,0}$ for a given temperature is necessary for this consideration. From this it also follows that $\Delta\theta_B \sim \sigma_{el,0}$ and $\Delta\theta_B \sim \Delta\sigma_{el}$ Duongthipthewa et al. [56] performed Raman spectroscopy at 488 nm excitation wavelength, in order to analyse the graphite structure of their CFRP test material. In addition, they investigated the electrical conductivity of their test material in various dimensions. Zhao et al. [54] reviewed the electrical conductivity and resistance of multiple stacked composite layers in all three dimensions. They also described the linear decrease of the electrical conductivity of CFRP when it is rotated from the angle of highest conductivity in the direction of the fibres to the orientation of lowest conductivity transverse to the direction of the fibres. Finally, Zhang et al. [57] demonstrated a linear correlation between the electrical and thermal conductivity of a carbon fibre for different temperatures. From their investigations, it can also be assumed that this relationship applies in a very similar way to a UD CFRP material. In order to verify their findings, they additionally compared their measurements with various other studies from the literature. This linear relationship between the rise in temperature and an increase in thermal conductivity was also confirmed by Oromiehie et al. [35].

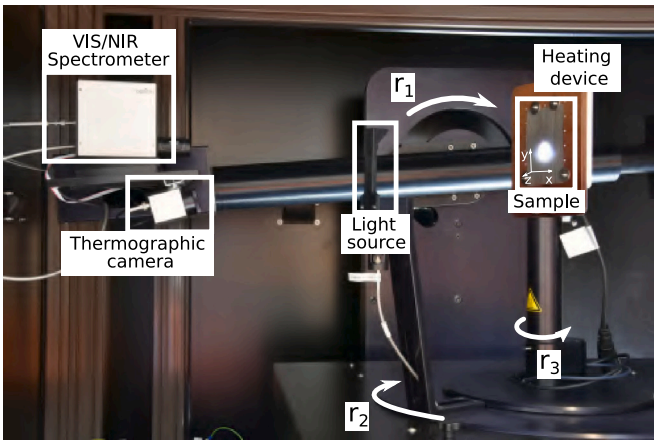

Fig. 4. Experimental setup Goniometer with VIS/NIR spectrometer and a thermographic camera. r_i denote the rotatable axes.

3. Methods

3.1. Experimental setup - Goniometer with heating element for VIS/NIR and FIR data acquisition

We utilised an Opsira GmbH Gonio'2pi-BSDF Custom Goniometer, [58] since it is particularly well suited for characterising optical material properties according to the literature in Section 2.3. With this device, the material Toray TC1225 T700/LM-PAEK with Toray T700 fibre [23] was measured at different temperatures $T = \{60, 140, 190, 230\}$ °C. This novel material is very promising for future use in the aerospace industry, hence we chose it for our tests. This material contains filaments with a diameter around 6.85 µm and a *Consolidated Ply Thickness* (CPT) of around 0.14 mm. Its glass transition temperature is $T_g = 147$ °C and the fibre volume ratio is about 66% [23]. The outlined approach for measuring and modelling is independent of the material type, but the optical properties are expected to vary for different materials and ambient temperatures. In this paper we only investigated the properties of the given material, since it is a rather novel material which is especially beneficial for utilisation in combination with the flashlamp heating technology in our application case. The setup is illustrated in Fig. 4. This Goniometer has two separate spectroradiometers installed for the VIS and NIR spectra. Consequently, these two spectrometers measured in the spectral bands from 300 nm to 1100 nm and 900 nm to 2400 nm, with a spectral resolution of about 1 nm. The area of overlap of both spectral ranges is used for stitching the spectra. Due to the stitching operation, there might be a deviation from the given resolution in the overlap area, which cannot be specified precisely, but needs to be taken into account. Every spectrometer wavelength measurement is digitalised by an individual 16-bit A/D conversion. The angular resolution of the rotating axes is

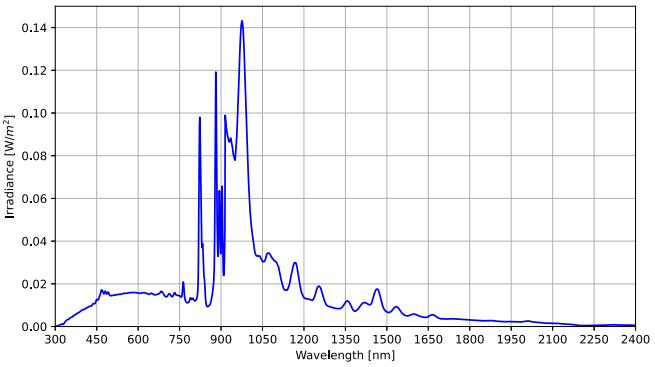

Fig. 5. Spectrum of the 125 W Osram XBO 150 W/CR OFR Xenon lamp [59] which was used as reference for the conducted experiments.

about 10^{-4}°. Considering the rotation of all axes, a spatial resolution of ≤0.03 mm is obtained. The operating distance of the specimen to the spectrometer lens was around 650 mm. The specimen was irradiated with a 125 W Osram XBO 150 W/CR OFR Xenon lamp [59] at a luminance of 20 000 cd/cm^2. The reference spectrum of this light which was used for our experiments is given in Fig. 5. This Xenon lamp has a rather similar spectral radiation characteristic as the Xenon flashlamp used for heating in the fibre placement process, presented in Fig. 1. The spot diameter of the illumination was about 25 mm. This spot size was chosen so that an integration across the spot area compensates for minor waviness and inhomogeneous fibre distributions in the specimen as well as for local differences in its scattering behaviour, but also so that the spot does not exceed the specimen dimensions even for large illumination angles. For specimen heating, the HAP 222 heating element from Hillesheim GmbH [60] was installed, which has a power consumption of up to 440 W at a maximum temperature of 250 °C. The temperature was controlled via the Hillesheim GmbH HT 60 controller [61] using a PT100 thermocouple as reference, which was located almost centred, just below the surface of the heating plate. The temperature deviation during control was about ±5 °C. However, we must note that the material sample was clamped onto the heating plate from the lateral edges and thus, there might be a small air filled gap of ≤0.5 mm between the heating plate and the specimen. In addition, the thermoplastic CFRP material has an insulating effect. Due to the air gap, which cannot be precisely monitored and the unknown thermal conductivity of the novel material, we assumed that the temperature on the material's surface was about 10–20 °C lower than the indicated temperature of the thermocouple. Due to these unknown influences, only relative relations are considered in this study and the absolute temperature values are only given as references.

Moreover, the sample was of course not illuminated during the thermographic measurements in order to avoid further heating and disturbing scattering effects.

In addition, we have installed an Optris PI 640 thermographic camera [19] to measure the thermal IR radiation in the wavelength range 7.5–13 µm. This sensor has a resolution of 640 × 480 px and a thermal sensitivity of 75 mK. For this measurement, the sensor recorded a 20 × 30 (width × height) measuring area in the centre of the sample. In this paper we only intend to investigate the relative emissivity of the material, without a direct estimation of the temperature and therefore, the configurable emissivity parameter of the sensor was set to $\epsilon = 1.0$. Since the exact emissivity of the novel material considered in this study is unknown, we have performed the calculation for this reference emissivity value. However, this does not correspond to a measured emissivity value of the material but is sufficient for the angle-based relative analysis in this paper.

For these measurements, the axis r_3 is rotated to the corresponding detection angle α in each case. Axis r_1 was rotated for the individual measurements in such a way that the spectroradiometer or the thermographic camera view was perpendicular to the labelled y-axis from Fig. 4 for each of the corresponding measurements. The r_2 rotation controls the respective illumination angle. The combined rotation of r_2 and r_3 defines the corresponding irradiance angle β with respect to the specimen's surface. All axes r_i were rotated around the centre of the specimen and thus, the optical axes of the sensors pointed to the specimen's centre at every rotation angle of r_i. The fibre angle γ was manually varied to either $\gamma = 0°$ or $\gamma = 90°$. These fibre orientations refer to the coordinate system in Fig. 4, where $\gamma = 0°$ describes a fibre orientation parallel to the x-axis and $\gamma = 90°$ specifies a fibre alignment along the y-axis. Please note that the stated measurement procedure is intended to determine comparative data for different CFRP materials. Since measurements are only taken in one plane per fibre orientation, out-of-plane scattering is not examined. We assume here that this out-of-plane scattering deviates only marginally between materials of a certain CFRP category.

3.2. Measurement of the temperature dependent optical material characteristics

3.2.1. Reflection analysis

First, a full scan of the fibre material sample was performed at a temperature of T = 60 °C, which was intended to examine the general reflection properties for the investigated, rather novel CFRP material. The measurement temperature of T = 60 °C is well suited for this purpose as it is reliably controllable and the cooler ambient air allows sufficient heat sink behaviour to prevent a severe temperature overshoot of the controller. Therefore, the accuracy of temperature control is around ±3 °C at ambient room temperature. Nevertheless, this temperature is still significantly below the glass transition temperature T_g = 147 °C of the material.

For this procedure the reflectance of the specimen ϱ_m for various detection, irradiation and fibre alignment angles was initially determined for the central VIS spectral range in the spectral band λ_{VIS} = [400 to 700] nm and for the central NIR spectrum between λ_{NIR} = [1300 to 1800] nm. To calculate the relative reflectance ϱ_m, the irradiance reflected from the material $E_{rm,\mathrm{OTB}}$ was normalised with the emitted irradiance of the light source. Note that the necessary, wavelength-dependent dark noise calibration was automatically carried out by the Goniometer for each individual measurement. Smaller temperature fluctuations in the ambient temperature are thus compensated for each measurement. For the conducted reflection observations, α was varied in the interval $[0, 80]°$ and β in the range $[0, 70]°$. The angle of observation α was rotated with a resolution of 1°. To reduce the measurement duration, the symmetry of the material was taken advantage of and thus, β was turned in increments of 5°. To determine the transmission characteristics, α and γ were varied as stated above.

Additionally, the relative intensity of the specular reflections of the full scan were plotted for the considered VIS and NIR spectral ranges. According to the findings discussed in Section 2.4.1 a Fresnel fitting was applied to the maxima and the corresponding characteristic values were investigated. This served to characterise the principle reflection characteristics of the novel material.

Subsequently, in a separate experiment, the specular reflections of the material were measured for the VIS and NIR spectral range. Therefore equal angles $\alpha = \beta$ in the interval [0,70]° with a step size of 10° were measured, for the different temperatures T = {60, 140, 190, 230} °C. These measurements were carried out for the fibre orientations $\gamma = 0°$ and $\gamma = 90°$. Assuming the reduced surface temperature deviation mentioned in Section 3.1, the given temperatures for this experiment are for $\ll T_g$, $\approx T_g$, $\gg T_g$. The measurements for each fibre orientation are carried out in order, starting from the lowest to the highest measurement temperature.

According to the literature referenced in Section 2.4.1, two meaningful attributes for specifying the reflectivity are the critical refractive index n_c and the Brewster angle θ_B. Both characteristic values were determined on the basis of the Fresnel fits and are indicated in the respective plots.

3.2.2. Emissivity analysis

In this section the methodology for investigating the angular dependent relative thermal emissivity in the FIR spectral band is outlined. The aim of this examination was the identification of potential differences in the angle dependent emission behaviour of the thermal FIR radiation for various material temperatures and filament orientations. For this purpose, the temperature of the specimen's surface was determined using a thermographic camera for the previously mentioned experimental temperatures, fibre orientations and viewing angles. Due to the unknown parameters and characteristics described in Section 3.1, the temperatures were normalised to the range of $[0, 1]$. Subsequently, a Fresnel fitting was again applied to the measurement results. Based on the findings from the related studies mentioned in Section 2.4.3, the individual components for the s- and p- polarisation are illustrated in addition to the effective Fresnel component the result plots.

3.2.3. Link between VIS/NIR reflectivity and FIR emissivity

From Section 2.4, we expect the Brewster angle to change linearly with the temperature. Accordingly, in addition to the previous analysis, the Brewster angles from the individual Fresnel fittings were visualised for the different VIS, NIR and FIR spectral regions and linear fittings were applied to the values of the Brewster angles for different temperatures. The gradient and the bias term of the linear fitting provide information about this assumption introduced above and the linkage between the individual spectral ranges.

For the analysis of these results, it should be noted that according to the findings from the literature in Section 2.4.4, a direct linear relationship exists between the change in Brewster angle and the change in electrical conductivity of the CFRP material. Furthermore, we know that the change in electrical conductivity is linearly correlated with the change in thermal conductivity of the CFRP. Thus, there is also a direct linear relationship between the change of the Brewster angle and the change of the thermal conductivity of the investigated CFRP material.

4. Results

4.1. VIS/NIR reflectivity full scan

The angular relative reflection values ϱ_m for the full scan and $T = 60$ °C are given in Fig. 6. Thus, ϱ_m is presented for various angles α and β in the VIS and NIR spectrum, each for the two considered fibre orientations. Figs. 6(a) and 6(b) show the measured values for the VIS band for a fibre orientation of $\gamma = 0°$. In Figs. 6(c) and 6(d) the results for the VIS spectrum and $\gamma = 90°$ are presented. Moreover, Figs. 6(e) and 6(f) present the measures for the NIR range and a fibre alignment of $\gamma = 0°$, and Figs. 6(g) and 6(h) give the findings for $\gamma = 90°$ in the NIR spectrum. For the sake of clarity, only the results for 5° detection increments are illustrated in the respective confusion matrices. The corresponding false colour plots present ϱ_m with a detailed resolution of 1°. The projected radiation is partially absorbed and reflected from the material while the transmitted radiation is assumed to be zero. As expected, the highest relative reflection is measured for $\alpha = \beta$ for both the VIS and NIR spectrum, which represent the direct, specular reflection. Due to the measurement resolution of 1° described above, optical scattering effects can lead to a slight clipping of the true peak value. However, these local effects should be very small, since integral measurements are performed over a comparatively wide light spot. Thus, for the measured values for $\alpha = \beta$ we assume, that the measured maxima are close to the true peak values and clipping effects are neglected in this study. As indicated in Fig. 6, ϱ_m for $\gamma = 0°$ varies between 0.32% and 2.42% in the VIS spectrum as well as between 0.07% to 0.71% in the NIR band. The diagonal elements for $\gamma = 90°$ are in the range of 0.27% up to 0.97% for VIS and 0.06% to 0.38% for NIR. These integral reflectance results were measured for the VIS band $\lambda_{VIS} = [400 \text{ to } 700]$ nm and for the NIR band $\lambda_{NIR} = [1300 \text{ to } 1800]$ nm, as described above. For both fibre orientations and spectral ranges, the ϱ_m values for $\alpha = \beta$ are quite constant up to 45°. For $\gamma = 0°$ these are in the range of 0.3% to 0.44% in VIS and 0.07% to 0.13% in NIR. For the sample rotation $\gamma = 90°$ these results are between 0.27% and 0.38% in VIS as well as 0.06% and 0.13% in NIR. For $\alpha = \beta > 45°$ the diagonal scores increase more quickly. Moreover, it is noticeable for $\gamma = 0°$ that there is an angular deviation of more than 5°, so that at $|\alpha - \beta| \geq 5°$ there is nearly no reflection measurable any more, but for $\gamma = 90°$, this variation is significantly larger. Furthermore, we can see that in the NIR plots in Figs. 6(e) and 6(g) a kind of noise appears. Especially in the area around the diagonal representing the specular reflection, this behaviour might also be attributed to scattering effects of the material which do not follow the cylinder reflection described in Section 2.4.1, since the wavelength range considered is already slightly within the order of magnitude of the filament diameter.

4.2. Specular reflection and Fresnel fitting VIS/NIR

In Fig. 7, the ϱ_m values discussed in the previous section are plotted along the illumination angles β in the range of $\beta = [10, 70]°$ in steps of 10°. This serves as a detailed analysis of the lateral reduction of the reflectance values. Fig. 7 presents the results for the fibre orientations of $\gamma = 0°$ and $\gamma = 90°$ again subdivided according to VIS and NIR spectral ranges.

The *full width at half maximum* (FWHM) is given as a reference. For the specimen rotation of $\gamma = 0°$, FWHM is in the range $\text{FWHM}_{VIS,0} = \text{FWHM}_{NIR,0} = [3, 4]°$ for the VIS and NIR bands for the displayed incidence angles β. For $\gamma = 90°$, however, FWHM varies in the interval $\text{FWHM}_{VIS,90} = [25, 56]°$ for VIS and $\text{FWHM}_{NIR,90} = [11, 68]°$ for NIR. Note, however, that the angular resolution for α is only 1°, which has to be taken into account and might cause minor errors of the FWHM value. The VIS plots clearly demonstrate the reflection pattern of a cylinder as outlined in Section 2.4.1. The NIR plots already show a slight deviation from this cylindrical curve shape, which might be due to the fact that the considered wavelength range is already in the order of magnitude of the filament diameter. However, the rough approximation to this mono-cylinder reflection is still visible. Please note that for $\gamma = 0°$, α and β are rotated in the plane given from the specimen normal and fibre direction. For $\gamma = 90°$, the detection and illumination angles are rotated in the normal plane perpendicular to the filament direction. Accordingly, the appearance of the curves given here differ from those shown in Fig. 3 by 90° for a specified γ and thus, a very narrow plot is obtained for $\gamma = 0°$ and a much wider curve for $\gamma = 90°$. The FWHM numbers clearly represent this relationship.

In Fig. 7, Fresnel curve fittings of the discrete peaks are plotted based on Eq. (4). The surrounding air in the measurement process is considered to have the ideal refractive index of $n_a = 1$. Accordingly, the refractive indexes of the CFRP n_c are estimated from the fitting parameters of the Fresnel plots and is given in the legends of the individual Figures. The refractive indexes differ for several fibre orientations and the two considered spectral intervals. This is because a non-isotropic material is observed. Therefore, the refractive index for $\gamma = 0°$ in the VIS range is $n_{c,0,VIS} = 1.29$ and in the NIR band $n_{c,0,NIR} = 1.27$. For a specimen angle of $\gamma = 90°$ the refractive index of $n_{c,90,VIS} = 1.64$ for VIS and $n_{c,90,NIR} = 1.39$ in the NIR spectrum. In addition, the Brewster angle θ_B of incidence can be approximated with the modified Snell's law from Eq. (3). However, this has to be understood as a rough estimate, as Snell's law actually only applies to isotropic materials and for the observation of objects much larger then the considered wavelength. Nevertheless, this provides insight into the strong rise of the Fresnel curve fittings for larger illumination angles. Thus, for $\gamma = 0°$ this gives $\theta_{B,0,VIS} = 52.15°$ in the VIS and $\theta_{B,0,NIR} = 51.83°$ in the NIR band as well as for $\gamma = 90°$, $\theta_{B,90,VIS} = 58.66°$ for VIS and $\theta_{B,90,NIR} = 54.31°$ for NIR.

In the following, the previously performed investigations of the Fresnel plots are repeated three times for each of the different temperatures $T = \{60, 140, 190, 230\}$ °C. The corresponding mean values

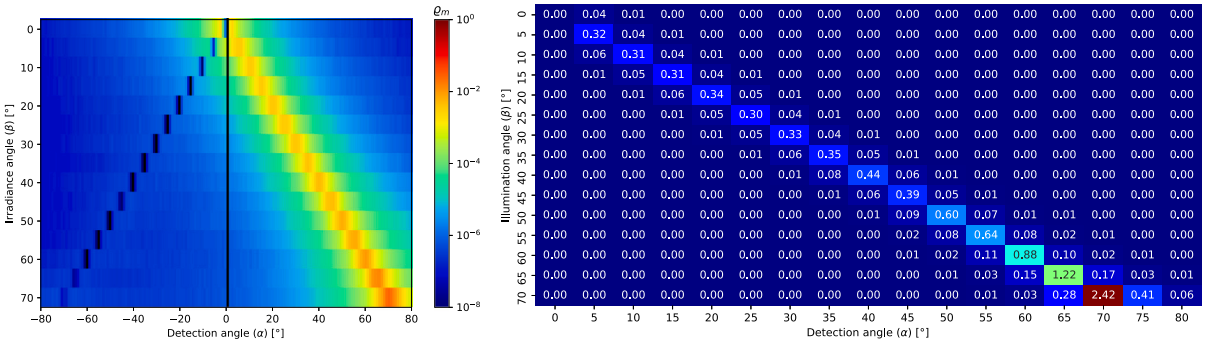

(a) Logarithm plot for the degree of reflection for the fibre orientation $\gamma = 0°$. Spectral range: 400-700 nm.

(b) Confusion matrix for the degree of reflection for the fibre orientation $\gamma = 0°$. The values are given in %. Spectral range: 400-700 nm.

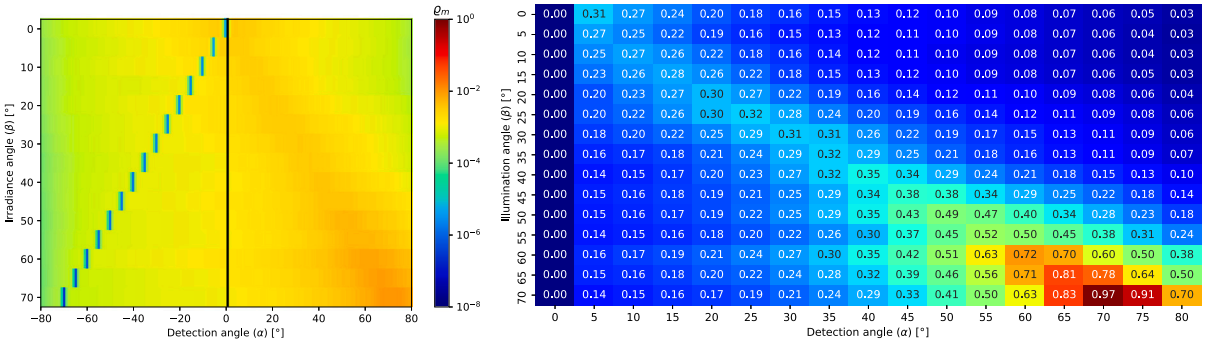

(c) Logarithm plot for the degree of reflection for the fibre orientation $\gamma = 90°$. Spectral range: 400-700 nm.

(d) Confusion matrix for the degree of reflection for the fibre orientation $\gamma = 90°$. The values are given in %. Spectral range: 400-700 nm.

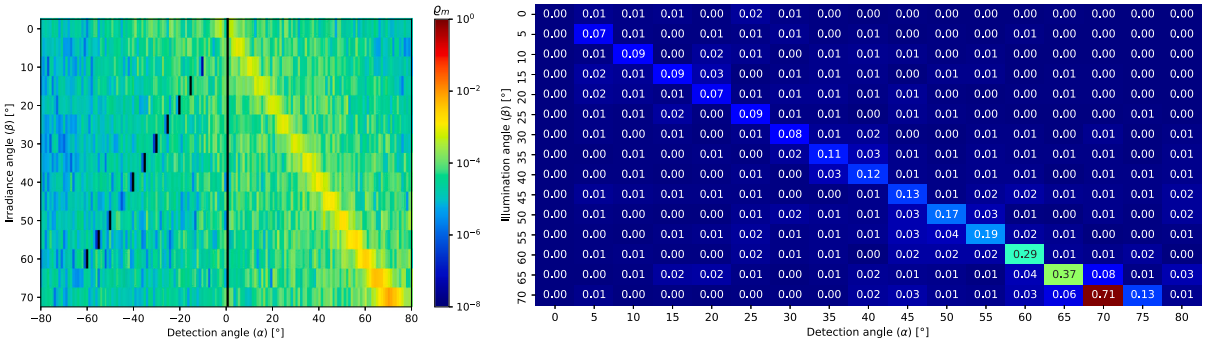

(e) Logarithm plot for the degree of reflection for the fibre orientation $\gamma = 0°$. Spectral range: 1300-1800 nm.

(f) Confusion matrix for the degree of reflection for the fibre orientation $\gamma = 0°$. The values are given in %. Spectral range: 1300-1800 nm.

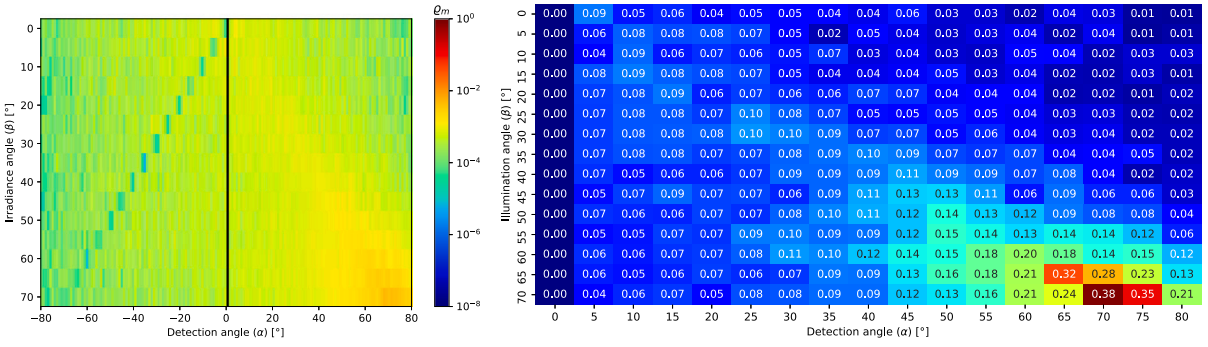

(g) Logarithm plot for the degree of reflection for the fibre orientation $\gamma = 90°$. Spectral range: 1300-1800 nm.

(h) Confusion matrix for the degree of reflection for the fibre orientation $\gamma = 90°$. The values are given in %. Spectral range: 1300-1800 nm.

Fig. 6. Reflection characteristics for the fibre orientations $\gamma = 0°$ and $\gamma = 90°$ for T = 60 °C.

together with their standard deviation as an error bar and the corresponding fittings of the effective Fresnel values are presented in Fig. 8. As before, the fibre orientations $\gamma = 0°$ and $\gamma = 90°$ as well as the VIS and NIR spectral ranges are considered. Again, the specular detection and illumination angle $\alpha = \beta$ is given on the abscissa and the percentage of reflection is presented on the ordinate.

When evaluating the results of the Fresnel fittings, for both spectral ranges, for the fibre orientation $\gamma = 0°$ an approximately linear decrease

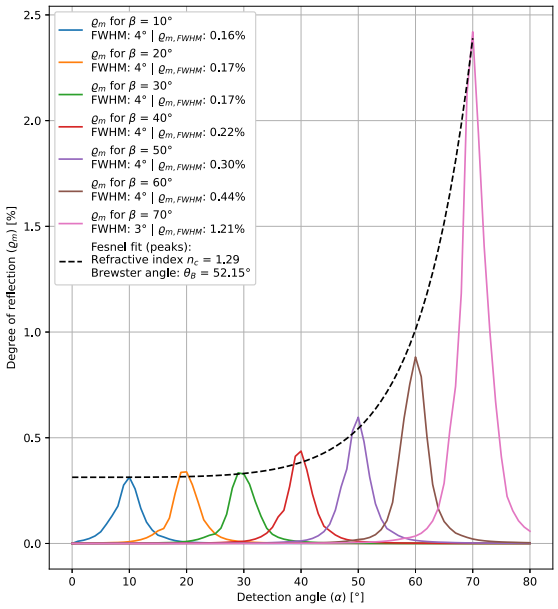

(a) Spectral reflectivity for $\alpha = \beta$ in range 10° to 70° for the fibre orientation $\gamma = 0°$, given in %. Spectral range: 400-700 nm.

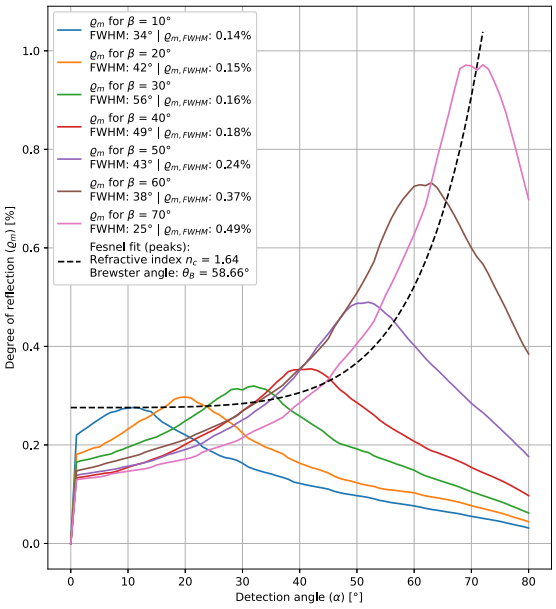

(b) Spectral reflectivity for $\alpha = \beta$ in range 10° to 70° for the fibre orientation for the fibre orientation $\gamma = 90°$, given in %. Spectral range: 400-700 nm.

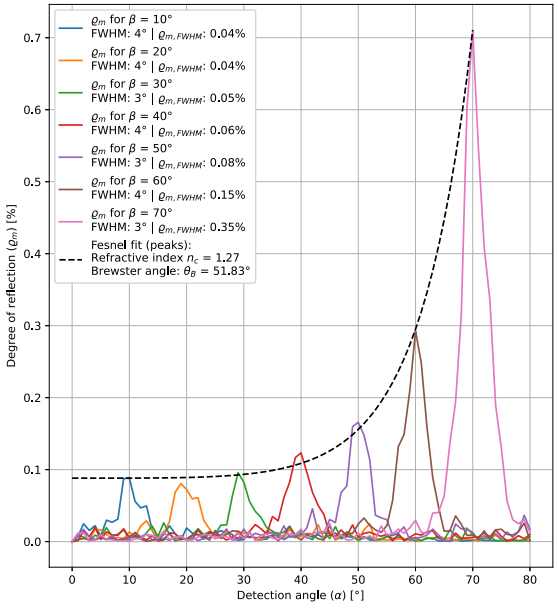

(c) Spectral reflectivity for $\alpha = \beta$ in range 10° to 70° for the fibre orientation $\gamma = 0°$, given in %. Spectral range: 1300-1800 nm.

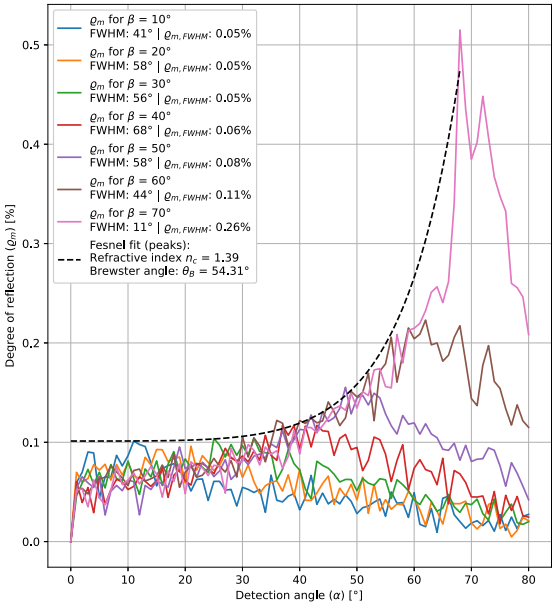

(d) Spectral reflectivity for $\alpha = \beta$ in range 10° to 70° for the fibre orientation for the fibre orientation $\gamma = 90°$, given in %. Spectral range: 1300-1800 nm.

Fig. 7. Spectral reflectivity $\beta = [10, 70]°$, together with the respective Fresnel fittings of the intensity peaks for T = 60 °C.

of the Brewster angle with increasing temperature is evident. The corresponding Brewster angles for the temperature range between $T = [60, 230]°$ in the VIS domain are in the interval $\theta_{B,0,VIS} = [51.18, 52.64]°$ and for the NIR between $\theta_{B,0,NIR} = [50.54, 53.77]°$. For $\gamma = 90°$, on the other hand, a slightly increasing trend of θ_B with increasing temperature can be recognised. In the VIS band θ_B varies between $\theta_{B,90,VIS} = [55.72, 56.83]°$ and in the NIR $\theta_{B,90,NIR} = [55.37, 57.44]°$.

The change of the Brewster angle with temperature in the different spectral ranges and the thermal emissivity variation are discussed in detail in the following section. The findings presented above provide the basis for these in depth analysis with respect to the reflectivity part of these investigations.

4.3. Change in emitted intensity in thermographic band

Fig. 9 shows the relative emissivities for different rotation angles of the specimen at various temperatures. The given values are normalised between 0 and 1. In contrast to the VIS and NIR spectral range, these normalised measurements for the various temperatures match with each other almost completely. In the considered FIR spectral range

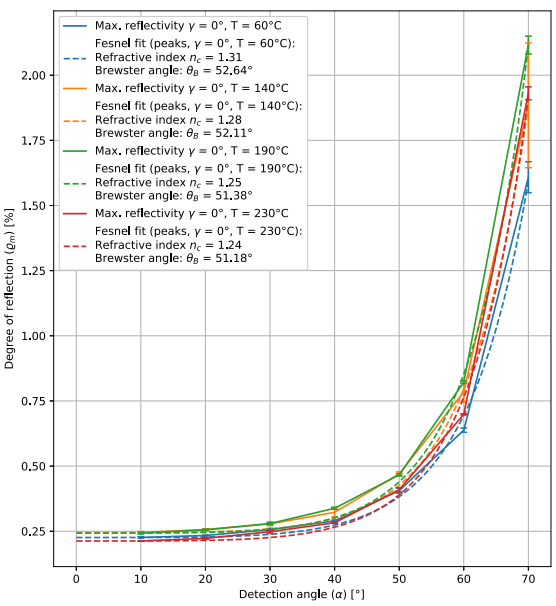

(a) Fresnel fit peaks - Spectral reflectivity for $\alpha = \beta$ in range 10° to 70° for the fibre orientation $\gamma = 0°$, given in %. Spectral range: 400-700 nm.

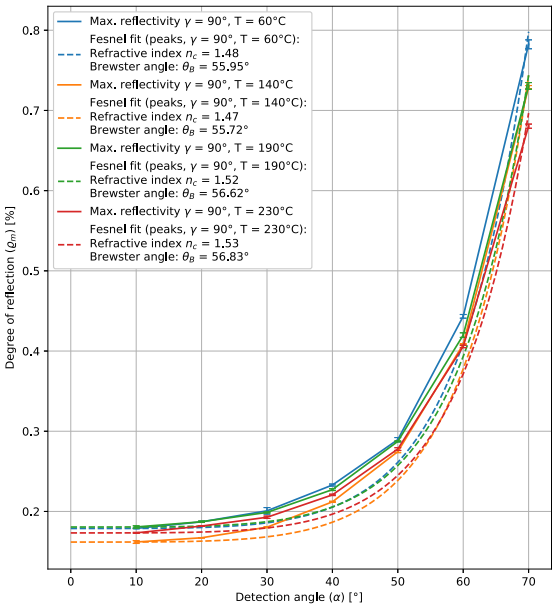

(b) Fresnel fit peaks - Spectral reflectivity for $\alpha = \beta$ in range 10° to 70° for the fibre orientation $\gamma = 90°$, given in %. Spectral range: 400-700 nm.

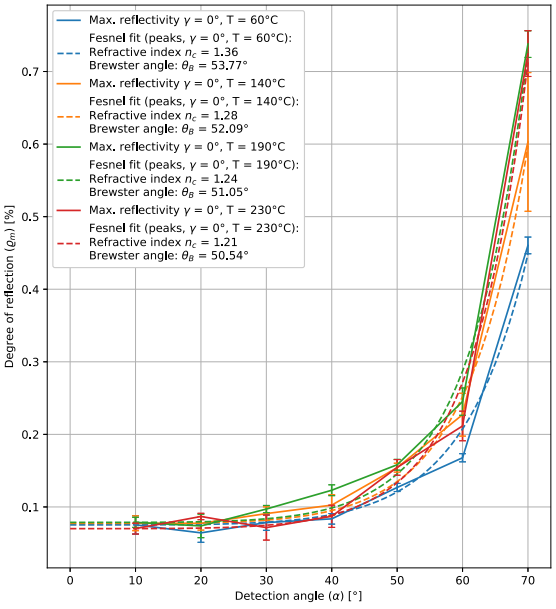

(c) Fresnel fit peaks - Spectral reflectivity for $\alpha = \beta$ in range 10° to 70° for the fibre orientation $\gamma = 0°$, given in %. Spectral range: 1300-1800 nm.

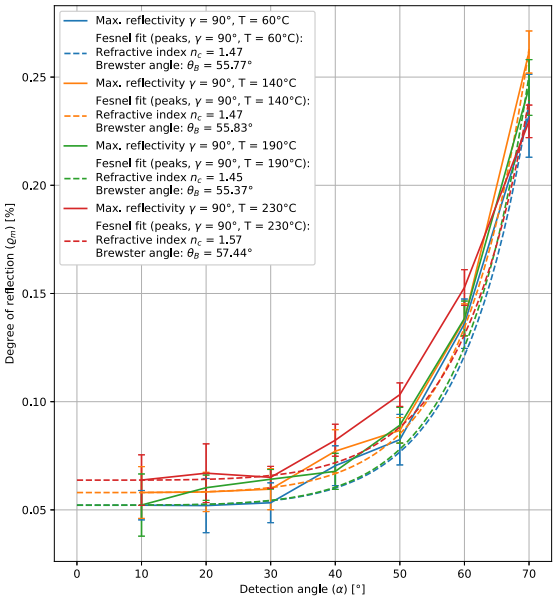

(d) Fresnel fit peaks - Spectral reflectivity for $\alpha = \beta$ in range 10° to 70° for the fibre orientation $\gamma = 90°$, given in %. Spectral range: 1300-1800 nm.

Fig. 8. Fresnel fit peaks — Spectral reflectivity $\beta = [10, 70]°$, together with the respective Fresnel fittings of the intensity peaks.

this corresponds to the expectations. An effective Fresnel fitting is applied to the plotted measured values and is represented as a dashed line. The dash–dot and dotted lines show the s- and p-polarised parts, respectively, of the effective Fresnel fit. The results are presented in Fig. 9(a) for $\gamma = 0°$ and in Fig. 9(b) for $\gamma = 90°$. The error bars represent the standard deviation across the multiple measurements per rotation angle.

The plots for both fibre orientations show a strong difference in the line shape of the plotted radiation intensities. Fig. 9(a) for the fibre orientation $\gamma = 0°$ follows the effective Fresnel fitting (- - -) relatively well, while however, a somewhat lower starting value is evident at the label (a.1). Subsequently, the radiation values increase up to an angle of rotation of about 40° and then drop sharply. In the starting range of the plot up to about 30° rotation angle, the influence of the p-polarised part of the Fresnel calculation is slightly predominant. According to the literature in Section 2.4.4, this lower initial values, which subsequently increase, indicate the presence of a conductive material. This is plausible, since the carbon fibres aligned in $\gamma = 0°$ are in principle conductive. Thus, this initial lower starting value is an indicator for the material's conductivity in this respective sample

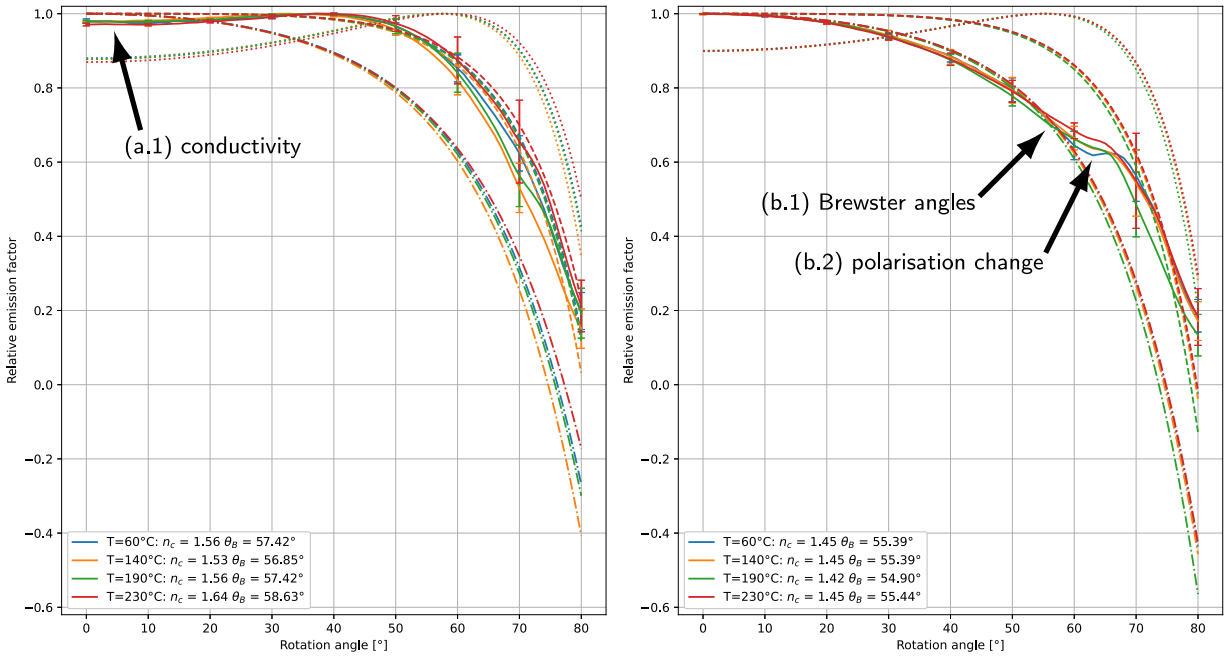

(a) Fresnel fits - Normalise thermal emissivity for the fibre orientation $\gamma = 0°$.

(b) Fresnel fits - Normalised thermal emissivity for the fibre orientation $\gamma = 90°$.

Fig. 9. Fresnel fits — Normalised thermal emissivity for different fibre orientation, in the domain $[0, 1]$. Data plots: (—); Fit. s-polarised: (– · – ·); Fit. p-polarised: (· · · · · ·); Fit. effective: (– – –).

orientation. Hence, this measurement method offers the possibility to evaluate the conductivity of the CFRP on the basis of radiated FIR emission.

The plots for the fibre orientation $\gamma = 90°$ in Fig. 9(b) reveal a rather different behaviour, as they follow the s-polarised part of the Fresnel fitting more closely, but only up to the Brewster angle at about 55° specimen rotation. Beyond this point, the curve is more similar to the effective Fresnel plot. Thus, this might indicate that the parallel aligned filaments in the CFRP specimen form a polarisation grating which polarises the radiated thermal radiation, as long as the viewing angle is $< \theta_B$. Hence, for the fibre orientation $\gamma = 90°$ there appears a polarisation effect, which is no longer significant above the Brewster angle. This is plausible since the filament diameter and the distance between the filaments are in the same order of magnitude as the FIR radiation and are thus potentially suitable as polarisers. Furthermore, $\gamma = 90°$ is considered here, so that the fibres are aligned parallel to the rotation axis and perpendicular to the plane in which the sensor is rotated and thus, the requirements for polarisation are fulfilled. In this context it is noteworthy, that polarisation is only possible on an electrically conductive grid, which again is an indicator for determining the conductivity of the CFRP material along the aligned carbon fibres.

In contrast to the fibre orientation $\gamma = 0°$, however, the maximum for $\gamma = 90°$ of the measured relative thermal radiation is at 0° rotation angle and afterwards the relative emission values decrease. This graph characteristic indicates that the s-polarised component of the Fresnel calculation dominates initially and from the Brewster angle onwards, both polarisation components have about the same proportion.

For $\gamma = 0°$ no significant polarisation effect is evident, which is also not expected, as the fibres are aligned perpendicular to the rotation axis, in the plane of the sensor rotation, and thus are not able to form a polarisation grating. The structure of the polymer chains in the thermoplastic matrix itself are presumably beyond the order of magnitude of the FIR radiation and thus have no significant polarisation effect in this wavelength band.

Based on the literature from Section 2.4.4, we also know that the electrical conductivity of the CFRP material changes with temperature. Since Fig. 9(b) implies that the Brewster angle is a corresponding indicator for this electrical conductivity of the CFRP material, this Brewster angle is plotted in Fig. 10 for the two fibre orientations $\gamma = 0°$ and $\gamma = 90°$ for the different spectral ranges VIS, NIR and FIR over various temperatures. As justified in Section 3.2 and given in Eq. (6) there is approximately a linear correlation between the electrical conductivity of CFRP and the temperature and thus, a linear fitting is applied to the individual plots. The fitting parameters are indicated in the legend, where the value m denotes the gradient of the linear line and the parameter b describes the ordinate intercept, which is the Brewster angle θ_B at T = 0 °C. For the interpretation of this figure we have to keep in mind, that the reflection measurements for VIS and NIR are carried out through active illumination from a certain direction and detection from the opposite direction. When measuring the thermal radiation in the FIR spectrum, the material is heated up and radiates heat. For the directional sensitivity in the considered application the results of the active and passive measurements are to be considered as rotated by 90° with respect to the fibre orientation. Hence, for the interpretation of FIR $\gamma = 0°$ we need to compare the values with the measures for $\gamma = 90°$ in VIS/NIR and vice versa.

We see that the gradients $\Delta\theta_{B,VIS}(\gamma = 90°)$, $\Delta\theta_{B,NIR}(\gamma = 90°)$ and $\Delta\theta_{B,FIR}(\gamma = 0°)$ are positive and they are each of the same order of magnitude. Thus, this indicates that the electrical conductivity σ_{el} along the carbon fibre increases with increasing temperature. On the other hand, for $\Delta\theta_{B,VIS}(\gamma = 0°)$, $\Delta\theta_{B,NIR}(\gamma = 0°)$ and $\Delta\theta_{B,FIR}(\gamma = 90°)$, a negative gradient in the change in Brewster angle is evident. This indicates that the conductivity of the thermoplastic CFRP material perpendicular to the fibre orientation decreases with increasing temperature. This is indeed plausible, as the polymer matrix expands with increasing temperature and the viscosity decreases. Thus, the individual fibres are pressed less strongly together, which reduces their conductivity in the composite as the temperature increases.

For these investigations we can write the previously introduced Eq. (6) as follows:

$$\frac{\sigma_{el,0}}{\epsilon_0 c} \approx 2\Delta\theta_B n_c^2 = 2\ mn_c^2 \tag{7}$$

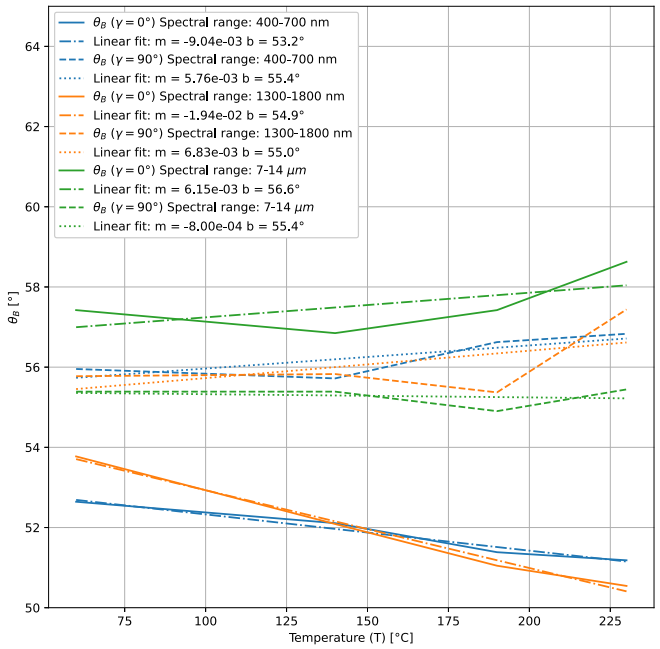

Fig. 10. Brewster angle θ_B for $\gamma = 0°$ and $\gamma = 90°$ for all investigated spectral ranges over different temperatures T.

To apply this equation, we have averaged the combined n_c values over the VIS and NIR, which is valid since the estimation in Eq. (6) is roughly similarly valid for the VIS and NIR spectral band. Furthermore, the values measured in our experiments are quite similar. Obviously, the calculations have been distinguished according to $\gamma = 0°$ and $\gamma = 90°$. Hence, for $\gamma = 0°$, the average refractive index is $\overline{n_{c,0}} = 1.25$ and for $\gamma = 90°$ this index is $\overline{n_{c,90}} = 1.5$. The refractive index of the surrounding air is assumed to be $n_a = 1$. With respect to the different $m = \Delta\theta_B$ values from Fig. 10 respectively for $\gamma = 0°$ the result interval is $\frac{\sigma_{el,0}}{\epsilon_0 c} \approx -[2.83, 6.06]\cdot 10^2$ and for $\gamma = 90°$ this yields $\frac{\sigma_{el,0}}{\epsilon_0 c} \approx [2.59, 3.07]\cdot 10^2$.

5. Discussion

In this study, we investigated the reflectivity and emissivity properties of the novel thermoplastic Toray TC1225 T700/LM-PAEK UD CFRP material via a Goniometer instrument. Initially, an observation of the full reflectivity behaviour of the material in the VIS and NIR spectrum at a constant temperature of T = 60 °C was carried out. Here, a strong difference in the reflection behaviour of the material with respect to the fibre orientation is evident, which agrees with the findings from the studies of Grouve [41] as well as Stokes-Griffin and Compston [42]. We also demonstrated that this characteristic behaviour is qualitatively rather similar for the VIS and NIR domains. However, the peak values of the relative reflectance in the NIR band are significantly lower than those in the VIS. Since the peak values for different viewing angles have a special significance for the characterisation of such material, these peak values of the relative reflection for different viewing angles were examined in detail. Since radiation in the VIS and NIR range is considered, these peak values for different viewing angles follow the effective Fresnel rule, which is in accordance with the findings from Le Louët et al. [16]. However, slight scattering effects are already recognisable for the reflection measurements in the NIR range, which might indicate a deviation from the cylindrical reflection model of Grouve [41] as well as Stokes-Griffin and Compston [42]. Here we have to mention that when considering a wavelength spectrum in the order of the filament diameter, further scattering effects can occur and the mono-cylinder reflection model is probably only valid to a limited extent. Moreover, we found that the critical refractive index n_c and the Brewster angle θ_B are quite helpful for the subsequent joined analysis of the emissivity and reflection behaviour. These values can be determined from the applied Fresnel fittings. For a fibre orientation of $\gamma = 0°$ we estimated a mean critical refraction index of $\overline{n_{c,0}} = 1.25$ and for $\gamma = 90°$ $\overline{n_{c,90}} = 1.5$. This also complements the results of Baho et al. [18] who only considered the refractive index and the reflection properties for a different thermoplastic material in the direction of the fibres for their heat propagation modelling.

Afterwards, we investigated the emissivity of the material in the FIR spectrum between 7–14 μm. Based on the investigations of Le Louët et al. [16] and Adibekyan et al. [17], we again applied a Fresnel fitting to the angle dependent FIR emissivity values. Therefore, we clearly recognise for the fibre orientation $\gamma = 0°$ indicators for analysing the conductivity of the material. In the perpendicular direction for $\gamma = 90°$ these effects are visible through the polarisability of the material. The general link to conductivity is already known from the fundamentals for other material types, [44] but nevertheless this is rather novel for CFRP. Moreover the very clear representation of the polarisation properties is not described in the literature, so far. According to these findings, we have compared the temperature-dependent Brewster angles for the different reflection and emission measurements, for the two fibre orientations $\gamma = \{0, 90\}°$. The study of Majérus et al. [55] has already shown a correlation between the Brewster angle and the electrical conductivity of a material and Wang et al. [53] as well as Mohiuddin and Hoa [52] have reported that the electrical conductivity of individual carbon fibres increases with increasing temperature. Based on this, we show in our investigations that for the conducted reflection and emission measurements, the Brewster angle increases with increasing temperature in the direction of the UD carbon fibres. Thus, we can indirectly estimate the increase in electrical conductivity along the fibre orientation using our previously describe approach. In contrast, transverse to the fibre orientation, a reduction of the Brewster angle and thus potentially a decrease in the electrical conductivity of the considered CFRP material with increasing temperature is found. The correlation between the gradient of the Brewster angle and the electrical conductivity presented from Majérus et al. [55] can be applied in our investigations to both, the VIS and NIR reflection measurements. Furthermore, Zhang et al. [57] reported a direct linear correlation between the electrical and the thermal conductivity of carbon fibres. Thus, the direction-dependent thermal conductivity in the UD CFRP material can also be evaluated through our presented approach. This means that our study and the relationships explained before provide a basis for a contactless and directional determination of the conductivity of CFRP material. Such a measurement technique can be used, for instance, in the fibre layup process to monitor the heat propagation within the material. For the actual heat propagation and conductivity modelling of multiple stacked CFRP plies the different CFRP fibre orientations need to be taken into account.

With respect to the first research question, we can summarise that the Fresnel fittings of the normalised emissivity and relative reflectivity values as well as the estimated Brewster angle are particularly well suited to characterise the thermoplastic Toray TC1225 T700/LM-PAEK UD CFRP material and to link the findings from the individual emission and reflection analyses via the direction-dependent electrical conductivity of the material.

Furthermore, referring to the second research question, the reflection measurements reveal that the maximum absorption of the Xenon spectrum is reached when the material is irradiated directly perpendicular to the surface. This changes only marginally up to an illumination angle of around 45°. The presented correlations between the reflection and emission behaviour to the electrical and thermal conductivity of the material can serve to improve the simulation of the heat propagation inside the CFRP material and to improve the direction-dependent irradiation of the CFRP material during the heating process. In addition, the measured normalised emissivity values can be used to directly adapt the adjustable emissivity coefficient for the

thermographic camera measurements to its viewing angle. This is particularly crucial for inline temperature monitoring in the AFP process, as the fibre material is often observed from a large and/or varying viewing angle.

In future research the validity of the applied conductivity correlations needs to be verified. Moreover, the change in emissivity and reflectivity with varying fibre volume fraction and porosity needs to be investigated. Furthermore, it is very interesting to examine the wavelength to filament diameter ratio up to which the described mono-cylinder reflection model is valid. Finally, we must also consider the possibility that the Xenon flashlamp itself has an influence on the inline measurement results of a thermographic camera due to its operating principle using high energy pulsed Xenon radiation for heating. This potentially disturbs the thermographic sensor and thus should also be investigated in more detail.

6. Conclusion

In this study we have characterised the optical properties of the novel thermoplastic Toray TC1225 T700/*Low Melt- Polyaryletherketone Carbon Fibre Reinforced Plastic* material. We have found that the application of Fresnel fitting is feasible to both reflectance measurements in the *Visible light* and *Near-Infrared* bands as well as emission measurements in the *Thermal-Infrared* domain. The Brewster angles derived from these fittings are very well suited to link these different analysis results and to make an estimate of the electrical and thermal conductivity behaviour of the *Carbon Fibre Reinforced Plastic* material for varying process temperatures. This means that our presented approach enables the analysis of the electrical and thermal conductivity of a *Carbon Fibre Reinforced Plastics* through its reflection and thermal radiation properties and thus, a contactless measurement of such conductivity characteristics is provided, which is very interesting for the process monitoring of heat propagation in fibre layup processes.

The results of our research are particularly valuable for manufacturers and users of heating systems operating in the spectral range between 400 nm and 1800 nm. Furthermore, the results are beneficial for operators of thermographic temperature measurement systems in composite inspection.

Future research needs to examine the influence of the fibre volume fraction and porosity of a deposited fibre material on its emissivity and reflectivity properties. Moreover, the validity of the mono-cylinder reflection model for other wavelengths and fibre diameters must be considered. In addition, the influence of the pulsed Xenon flashlamp on the thermographic measurements should be investigated.

CRediT authorship contribution statement

Sebastian Meister: Conceptualisation; Methodology; Software; Formal analysis; Investigation; Writing - Original Draft. **Andreas Kolbe:** Conceptualisation; Writing - Original. **Roger M. Groves:** Methodology; Writing - Review & Editing; Supervision.

Acknowledgement

All authors have approved the final manuscript.

Funding

The research was carried out within the framework of the German Aerospace Center's core funded research.

Declaration of competing interest

The authors declare that they have no known competing financial interests or personal relationships that could have appeared to influence the work reported in this paper.

References

[1] Marsh G. Airbus a350 XWB update. Reinf Plast 2010;54(6):20–4. http://dx.doi.org/10.1016/s0034-3617(10/70212-5.

[2] McIlhagger A, Archer E, McIlhagger R. Manufacturing processes for composite materials and components for aerospace applications. In: Irving P, Soutis C, editors. Polymer composites in the aerospace industry. Elsevier; 2020, p. 59–81. http://dx.doi.org/10.1016/b978-0-08-102679-3.00003-4.

[3] Meister S, Möller N, Stüve J, Groves RM. Synthetic image data augmentation for fibre layup inspection processes: Techniques to enhance the data set. J Intell Manuf 2021. http://dx.doi.org/10.1007/s10845-021-01738-7.

[4] Parmar H, Khan T, Tucci F, Umer R, Carlone P. Advanced robotics and additive manufacturing of composites: towards a new era in Industry 4.0. Mater Manuf Process 2021;1–35. http://dx.doi.org/10.1080/10426914.2020.1866195.

[5] Brecher C, Kermer-Meyer A, Stimpfl J, Emonts M. Load-optimised tailored thermoplastic FRP blanks for mass production. JEC Compos Mag 2011;48(65):60–2.

[6] Pegoretti A. Towards sustainable structural composites: A review on the recycling of continuous-fiber-reinforced thermoplastics. Adv Ind Eng Polym Res 2021;4(2):105–15. http://dx.doi.org/10.1016/j.aiepr.2021.03.001.

[7] Francesco MD, Veldenz L, Dell'Anno G, Potter K. Heater power control for multi-material, variable speed Automated Fibre Placement. Composites A 2017;101:408–21. http://dx.doi.org/10.1016/j.compositesa.2017.06.015.

[8] Schiel I, Raps L, Chadwick AR, Schmidt I, Simone M, Nowotny S. An investigation of in-situ AFP process parameters using CF/LM-PAEK. Adv Manuf: Polym Compos Sci 2020;6(4):191–7. http://dx.doi.org/10.1080/20550340.2020.1826772.

[9] Danezis A, Williams D, Edwards M, Skordos A. Heat transfer modelling of flashlamp heating for automated tape placement of thermoplastic composites. Composites A 2021;106381. http://dx.doi.org/10.1016/j.compositesa.2021.106381.

[10] Lascelles P. humm3 - our journey to industrialisation. Tech. rep., Heraeus Noblelight Ltd.; 2020, URL https://www.heraeus.com/media/media/hng/doc_hng/industries_and_applications_1/arc_and_flash_applications_1/humm3_-_our_journey_to_industrialisation.pdf.

[11] Superior Quartz Products Inc. Xenon short arc lamps - lamp characteristics & description. techreport, Superior Quartz Products Inc.; 2021, URL https://www.sqpuv.com/PDFs/TechnicalSpecificationGuide.pdf.

[12] Denkena B, Schmidt C, Völtzer K, Hocke T. Thermographic online monitoring system for automated fiber placement processes. Composites B 2016;97:239–43. http://dx.doi.org/10.1016/j.compositesb.2016.04.076.

[13] Chen M, Jiang M, Liu X, Wu B. Intelligent inspection system based on infrared vision for automated fiber placement. In: 2018 IEEE international conference on mechatronics and automation (ICMA). IEEE; 2018, http://dx.doi.org/10.1109/icma.2018.8484646.

[14] Gregory ED, Juarez PD. In-situ thermography of automated fiber placement parts. In: AIP conference proceedings. 2018, http://dx.doi.org/10.1063/1.5031551.

[15] Sun S, Han Z, Fu H, Jin H, Dhupia JS, Wang Y. Defect characteristics and online detection techniques during manufacturing of FRPs using automated fiber placement: A review. Polymers 2020;12(6):1337. http://dx.doi.org/10.3390/polym12061337.

[16] Le Louët V, Rousseau B, Corre SL, Boyard N, Tardif X, Delmas J, Delaunay D. Directional spectral reflectivity measurements of a carbon fibre reinforced composite up to 450 °C. Int J Heat Mass Transfer 2017;112:882–90. http://dx.doi.org/10.1016/j.ijheatmasstransfer.2017.04.125.

[17] Adibekyan A, Kononogova E, Monte C, Hollandt J. Review of PTB measurements on emissivity, reflectivity and transmissivity of semitransparent fiber-reinforced plastic composites. Int J Thermophys 2019;40(4). http://dx.doi.org/10.1007/s10765-019-2498-0.

[18] Baho O, Ausias G, Grohens Y, Barile M, Lecce L, Férec J. Automated fibre placement process for a new hybrid material: A numerical tool for predicting an efficient heating law. Composites A 2021;144:106360. http://dx.doi.org/10.1016/j.compositesa.2021.106360.

[19] Optris GmbH. optris PI 640 - technical data. Optris GmbH; 2021, URL https://www.optris.co.uk/thermal-imager-optris-pi-640 (accessed: 04 May 2021).

[20] Assadi M. High speed afp processing of thermoplastics. techreport, Electroimpact Inc.; 2021.

[21] Denkena B, Schmidt C, Weber P. Automated fiber placement head for manufacturing of innovative aerospace stiffening structures. Proc Manuf 2016;6:96–104. http://dx.doi.org/10.1016/j.promfg.2016.11.013.

[22] Boon YD, Joshi SC, Bhudolia SK. Review: filament winding and automated fiber placement with in situ consolidation for fiber reinforced thermoplastic polymer composites. Polymers 2021;13(12):1951. http://dx.doi.org/10.3390/polym13121951.

[23] Toray. Toray cetex TC1225 - LMPAEK. techreport v5, Toray; 2020, URL https://www.toraytac.com/media/3bd72fac-0406-48e4-bfc4-2ffd2398ac0c/zipxIA/TAC/Documents/Data_sheets/Thermoplastic/UDtapes.prepregsandlaminates/Toray-Cetex-TC1225_PAEK_PDS.pdf (accessed: 2021-05-28).
[24] Rosselli F, Santare MH, Güçeri SI. Effects of processing on laser assisted thermoplastic tape consolidation. Composites A 1997;28(12):1023–33. http://dx.doi.org/10.1016/s1359-835x(97/00072-9.
[25] Pistor C, Yardimci M, Güçeri S. On-line consolidation of thermoplastic composites using laser scanning. Composites A 1999;30(10):1149–57. http://dx.doi.org/10.1016/s1359-835x(99/00030-5.
[26] Goodman D, Byrne C, Yen A, Moulton R, Dixon D, Costen R. Automated tape placement with in-situ electron beam cure. Sampe J 2000;36:11–7.
[27] Luinge H. Processing of thermoplastic composites; developments & future challenges. In: IHTEC bremen 2018. Nijverdal, The Netherlands: TenCate Advanced Composites; 2018.
[28] Stokes-Griffin CM, Compston P, Matuszyk TI, Cardew-Hall MJ. Thermal modelling of the laser-assisted thermoplastic tape placement process. J Thermoplast Compos Mater 2015;28(10):1445–62. http://dx.doi.org/10.1177/0892705713513285.
[29] Tierney J, Gillespie JW. Modeling of heat transfer and void dynamics for the thermoplastic composite tow-placement process. J Compos Mater 2003;37(19):1745–68. http://dx.doi.org/10.1177/0021998303035188.
[30] Hosseini SMA, Baran I, van Drongelen M, Akkerman R. On the temperature evolution during continuous laser-assisted tape winding of multiple C/PEEK layers: The effect of roller deformation. Int J Mater Form 2020;14(2):203–21. http://dx.doi.org/10.1007/s12289-020-01568-7.
[31] Hörmann P, Stelzl D, Lichtinger R, Nieuwenhove SV, Carro GM, Drechsler K. On the numerical prediction of radiative heat transfer for thermoset automated fiber placement. Composites A 2014;67:282–8. http://dx.doi.org/10.1016/j.compositesa.2014.08.019.
[32] Brown M, Monnot P, Williams D. Developments in xenon flashlamp heating for automated fibre placement. In: Automated composites manufacturing. 2019.
[33] Monnot P, Williams D, Francesco MD. Power control of a flashlamp-based heating solution for automated dry fibre placement. In: ECCM18. 2018.
[34] Usamentiaga R, Venegas P, Guerediaga J, Vega L, Molleda J, Bulnes F. Infrared thermography for temperature measurement and non-destructive testing. Sensors 2014;14(7):12305–48. http://dx.doi.org/10.3390/s140712305.
[35] Oromiehie E, Chakladar N, Rajan G, Prusty B. Online monitoring and prediction of thermo-mechanics of AFP based thermoplastic composites. Sensors 2019;19(6):1310. http://dx.doi.org/10.3390/s19061310.
[36] Rabal AM, Ferrero A, Campos J, Fontecha JL, Pons A, no AMR, Corróns A. Automatic gonio-spectrophotometer for the absolute measurement of the spectral BRDF at in- out-of-plane and retroreflection geometries. Metrologia 2012;49(3):213–23. http://dx.doi.org/10.1088/0026-1394/49/3/213.
[37] Martinez ML, Hartmann T. Multispectral gonioreflectometer facility for directional reflectance measurements and its use on materials and paints. In: Stein KU, Schleijpen R, editors. Target and background signatures iv. SPIE; 2018, http://dx.doi.org/10.1117/12.2325711.
[38] Li H, Chen M, Deng C, Liao N, Rao Z. Versatile four-axis gonioreflectometer for bidirectional reflectance distribution function measurements on anisotropic material surfaces. Opt Eng 2019;58(12):1. http://dx.doi.org/10.1117/1.oe.58.12.124106.
[39] Xu H, Hu J, Yu Z. Absorption behavior analysis of carbon fiber reinforced polymer in laser processing. Opt Mater Express 2015;5(10):2330. http://dx.doi.org/10.1364/ome.5.002330.
[40] Schmitt R, Orth A, Niggemann C. A method for edge detection of textile preforms using a light-section sensor for the automated manufacturing of fibre-reinforced plastics. In: Osten W, Gorecki C, Novak EL, editors. Optical measurement systems for industrial inspection v. SPIE; 2007, http://dx.doi.org/10.1117/12.726177.
[41] Grouve W. Weld strength of laser-assisted tape-placed thermoplastic composites (Ph.D. thesis), University of Twente; 2012, http://dx.doi.org/10.3990/1.9789036533928.
[42] Stokes-Griffin C, Compston P. Optical characterisation and modelling for oblique near-infrared laser heating of carbon fibre reinforced thermoplastic composites. Opt Lasers Eng 2015;72:1–11. http://dx.doi.org/10.1016/j.optlaseng.2015.03.016.
[43] Kasap S, Capper P. Springer handbook of electronic and photonic materials. 2nd ed.. Springer International Publishing; 2017, http://dx.doi.org/10.1007/978-3-319-48933-9,
[44] Vollmer M, Möllmann K-P. Infrared thermal imaging - 2nd edition. 2nd ed.. John Wiley and Sons; 2018, URL https://www.wiley.com/en-us/InfraredThermalImaging.
[45] Dombrovsky LA. Thermal radiation from nonisothermal spherical particles. Begell House; 2011, http://dx.doi.org/10.1615/thermopedia.000141, URL https://thermopedia.com/content/141/ (accessed: 30 April 2021).
[46] Warren TJ, Bowles NE, Hanna KD, Bandfield JL. Modeling the angular dependence of emissivity of randomly rough surfaces. J Geophys Res: Planets 2019;124(2):585–601. http://dx.doi.org/10.1029/2018je005840.
[47] Li X, Strieder W. Emissivity of high-temperature fiber composites. Ind Eng Chem Res 2009;48(4):2236–44. http://dx.doi.org/10.1021/ie8008583.
[48] Nunak N, Roonprasang K, Suesut T, Nunak T. Emissivity estimation using thermographic camera. Adv Mater Res 2013;811:380–7. http://dx.doi.org/10.4028/www.scientific.net/amr.811.380.
[49] Tomboulian BN, Hyers RW. Predicting the effective emissivity of an array of aligned carbon fibers using the reverse Monte Carlo ray-tracing method. J Heat Transfer 2016;139(1). http://dx.doi.org/10.1115/1.4034310.
[50] Golyk VA, Krüger M, Kardar M. Heat radiation from long cylindrical objects. Phys Rev E 2012;85(4). http://dx.doi.org/10.1103/physreve.85.046603.
[51] Ebbesen TW, Lezec HJ, Hiura H, Bennett JW, Ghaemi HF, Thio T. Electrical conductivity of individual carbon nanotubes. Nature 1996;382(6586):54–6. http://dx.doi.org/10.1038/382054a0.
[52] Mohiuddin M, Hoa S. Temperature dependent electrical conductivity of CNT–PEEK composites. Compos Sci Technol 2011;72(1):21–7. http://dx.doi.org/10.1016/j.compscitech.2011.08.018.
[53] Wang Y, Ramos I, Furlan R, Santiago-Aviles J. Electronic transport properties of IncipientGraphitic domains formation in PAN derived carbon nanofibers. IEEE Trans Nanotechnol 2004;3(1):80–5. http://dx.doi.org/10.1109/tnano.2004.824036.
[54] Zhao Q, Zhang K, Zhu S, Xu H, Cao D, Zhao L, Zhang R, Yin W. Review on the electrical resistance/conductivity of carbon fiber reinforced polymer. Appl Sci 2019;9(11):2390. http://dx.doi.org/10.3390/app9112390.
[55] Majérus B, Cormann M, Reckinger N, Paillet M, Henrard L, Lambin P, Lobet M. Modified brewster angle on conducting 2D materials. 2D Mater 2018;5(2):025007. http://dx.doi.org/10.1088/2053-1583/aaa574.
[56] Duongthipthewa A, Su Y, Zhou L. Electrical conductivity and mechanical property improvement by low-temperature carbon nanotube growth on carbon fiber fabric with nanofiller incorporation. Composites B 2020;182:107581. http://dx.doi.org/10.1016/j.compositesb.2019.107581.
[57] Zhang X, Fujiwara S, Fujii M. Measurements of thermal conductivity and electrical conductivity of a single carbon fiber. Int J Thermophys 2000;21(4):965–80. http://dx.doi.org/10.1023/a:1006674510648.
[58] Opsira GmbH. gonio'2pi. techreport, Leibnizstraße 20, 88250 Weingarten, Germany: Opsira GmbH; 2019, URL https://www.opsira.de/fileadmin/benutzerdaten/opsira-de/pdf/Product_information_near-field_goniophotometer_gonio_2pi_-_E_-_V00263114_-_opsira.pdf.
[59] OSRAM GmbH. XBO 150 W/CR OFR. techreport, OSRAM GmbH; 2021, URL https://www.osram.com/ecat/XBOXenonshort-arclampswithoutreflector-XBOXenonshort-arclamps-Dischargelamps-Industry-SpecialtyLighting/com/en/GPS01_1028545/ZMP_56399/.
[60] Hillesheim GmbH. Aluminium electric heating plate. Hillesheim GmbH; 2021, URL https://www.hillesheim-gmbh.com/en/products/aluminium-electric_heating_plate.php (accessed: 04 May 2021).
[61] Hillesheim GmbH. Electronic controller - HT 63 series. Hillesheim GmbH; 2021, URL https://www.hillesheim-gmbh.com/en/products/product.php?id=167 (accessed: 04 May 2021).

Sebastian Meister is a PhD Candidate in optical inspection at the Delft University of Technology, The Netherlands, at the Aerospace Non-Destructive Testing Laboratory. He is also working as a Researcher at the German Aerospace Center, Center for Lightweight-Production-Technology in Stade, Germany. In 2017 he received his Master's degree in Mechanical Engineering from Friedrich-Alexander-University of Erlangen-Nürnberg. His fields of research are computer vision and machine learning for the optical inspection in automated composite manufacturing.

Andreas Kolbe is working as a researcher at the German Aerospace Center, Institute of Composite Structures and Adaptive Systems, Center for Lightweight Production Technologies in Stade. In 2012 he received his Master's degree in Resource Efficient Technologies and Processes at Mechanical Engineering Department of the University Wismar. His research interest are heating technologies for the Automated Fibre Placement of composites.

Dr. Roger M. Groves is Associate Professor in Aerospace NDT/SHM and Heritage Diagnostics at Delft University of Technology, The Netherlands. His PhD is in Optical Instrumentation from Cranfield University (2002) and he was a Senior Scientist at the Institute for Applied Optics, University of Stuttgart, before joining TU Delft in 2008 as an Assistant Professor. Dr Groves heads a team of approximately 20 researchers in the Aerospace NDT Laboratory at TU Delft. His research interests are Optical Metrology, Fibre Optic Sensing and Ultrasonic Wave Propagation in Composite Materials. He has approximately 200 journal and conference publications in these topics. In 2020 he was awarded Fellow of SPIE.